Marine Geology 421 (2020) 106062

Contents lists available at ScienceDirect

Marine Geology

journal homepage: www.elsevier.com/locate/margo

An integrated optic and acoustic (IOA) approach for measuring suspended sediment concentration in highly turbid environments

Jianliang Lin[a,b], Qing He[a,*], Leicheng Guo[a], Bram C. van Prooijen[b], Zheng Bing Wang[a,b,c]

[a] State Key Laboratory of Estuarine and Coastal Research, East China Normal University, Shanghai 200241, China
[b] Faculty of Civil Engineering and Geosciences, Delft University of Technology, Delft, the Netherlands
[c] Deltares, Delft, the Netherlands

ARTICLE INFO

Editor: Edward Anthony

Keywords:
Suspended sediment concentration
Optical Backscatter Sensor
Argus Suspension Meter
Acoustic Doppler Velocimeter
Concentrated benthic suspension

ABSTRACTS

Accurate measurement of suspended sediment concentration (SSC) in highly turbid environments has been a problem due to optical or acoustic signal saturation and attenuation. The saturation returns a limited measurement range, and the attenuation raises an ambiguity problem that a low optical or acoustic output could mean a low or a high SSC. In this study, an integrated optic and acoustic (IOA) approach is proposed to (i) overcome the ambiguity problem; (ii) increase the measurement range to high SSC values; and (iii) obtain high-resolution SSC profiles. The IOA approach is a combination of Argus Suspension Meter (ASM), Optical Backscatter Sensor (OBS) and Acoustic Doppler Velocimeter (ADV). In this approach, the ASM-derived SSC is preferred because of its lowest relative error, followed by OBS and ADV. The ASM can produce high-resolution (1 cm interval) SSC profiles when it is not saturated (usually SSC < 9 g/L). When ASM is saturated, the SSC is recovered by OBS. Since the ambiguity problem is solved, the measurement range of OBS and ADV can be extended up to 300 g/L. The best way to use an ADV, however, is to have a rough estimation first and assist in the OBS conversion, because its estimates contain large uncertainty. To further mitigate the impact of sediment particle size on SSC retrieval, we suggest the usage of in-situ sediment samples for sensor calibration. The IOA approach was verified in the Yangtze Estuary which is a highly turbid system. Comparison of the IOA approach outputs against water sampling results demonstrates the reliability of the IOA approach with a relative error of 17–34%. The observed high SSCs were up to 63 g/L. The field data show that high SSCs were confined in the benthic layer (within 2 m above the bed) in the wet season under a high river discharge, whereas the suspension was better mixed throughout the water column in the dry season.

1. Introduction

Suspended sediment concentration (SSC) is a critical parameter for understanding the transport of sediment and associated contaminants (Manning et al., 2010; Liang et al., 2013; Huettel et al., 2014; Burchard et al., 2018). SSC also limits the light availability and affects the primary production in lakes, rivers, estuaries and coastal waters (Yoshiyama and Sharp, 2006; Van Kessel et al., 2011). SSC can vary orders of magnitude over a small distance or a short period (Burchard et al., 2018; Ge et al., 2018). Accurate SSC measurements with a high spatial and temporal resolution, therefore, have significant implications for the management of ecology, biogeochemistry, and geomorphology. However, measuring high-resolution SSC in a simple, robust and efficient way is not straightforward (Table 1), particularly in highly turbid environments.

Water sampling (e.g., suction/pumping) is a traditional, reliable and widely used method to measure SSC. The SSC from the water sample is generally regarded as a reference for sensor calibration (Kineke and Sternberg, 1992; Fugate and Friedrichs, 2002; Gray and Gartner, 2010; Wang et al., 2013; Baeye and Fettweis, 2015; Druine et al., 2018). The SSC given by this method contains a relative error of ~20% from sampling and later analysis (McHenry et al., 1967). Point-integrating samplers can obtain SSC profiles of nearly the entire water column. However, water sampling is labor-intensive, implying that both temporal and spatial resolutions are generally limited. Accurate near-bed sampling (< 0.5 m) is furthermore challenging, although this region is of high interest for understanding sediment exchange processes.

To obtain high-resolution SSC profile, especially in the bottom boundary layer, more advanced technologies and sensors (optical or acoustic) have been developed in the last decades (Wren et al., 2000;

* Corresponding author.
E-mail address: qinghe@sklec.ecnu.edu.cn (Q. He).

https://doi.org/10.1016/j.margeo.2019.106062
Received 18 December 2018; Received in revised form 30 August 2019; Accepted 1 October 2019
Available online 21 October 2019
0025-3227/

Table 1
Measurement techniques of suspended sediment concentration.

Technology	Operating principle	Advantages	Disadvantages
Water sampling	Water-sediment sample is taken and later analyzed	Reliable Informative (SSC, salinity, PSD[a] etc.)	Flow-intrusive Labor-intensive Low frequency Poor spatial resolution Near-bed data missing
Optical	Light backscatter through water-sediment sample is measured and translated to SSC with calibration	High accuracy Good spatial resolution High frequency	Flow-intrusive Particle-size dependent Limit measurement range Uncertainties in high SSC
Acoustic	Echo strength from sample determines SSC based on calibration	Nonintrusive Good spatial resolution High frequency synchronous SSC and velocity	Low accuracy Limit measurement range Uncertainties in high SSC

[a] SSC and PSD denote suspended sediment concentration and particle size distribution, respectively.

Thorne and Hanes, 2002; Rai and Kumar, 2015; Rymszewicz et al., 2017).

Optical sensors measure SSC by the strength of back- or side-scattered light, e.g., Optical Backscatter Sensor (OBS) (Campbell Scientific, 2018), Argus Suspension Meter (ASM) (Argus, 2014), YSI (YSI Incorporated, 2012), Fiber Optic In-stream Transmissometer (FIT) (Campbell et al., 2005) and HHU-LIOS (Shao and Maa, 2017). They can measure SSC at a high frequency (1–25 Hz) (Campbell Scientific, 2018), but their measurements are generally restricted to a single point in a fixed deployment. Stacked optical sensors (e.g., Argus Suspension Meter, ASM) were later developed and provide SSC profile with a vertical resolution of 1 cm (Vijverberg et al., 2011; Ge et al., 2018). Although multiple or moving optical sensors increase the spatial resolution of SSC measurements, they still require an intrusion in the flow, which may disturb the flow as well as the distribution of suspended sediment. Particle-size dependency is another drawback of the optical sensor. The reading of the same sensor may increase by as much as ten times for the same SSC with a smaller particle size (Ludwig and Hanes, 1990; Campbell Scientific, 2018). Therefore, continuous calibration against in-situ SSC from water sampling is needed (Maa et al., 1992; Nauw et al., 2014). Additionally, the optical output has an upper limit, because of the signal saturation (e.g., ASM) or attenuation (e.g., OBS). Within a low SSC (< 9 g/L), optical output increases nearly linearly with increasing SSC (Fig. 1, see also Downing, 2006; Shao and Maa, 2017). Beyond the threshold, however, ASM output maintains at its maximum, and OBS output decreases with increasing SSC (Fig. 1). As a result, ASM has a limited measurement range, and OBS has an ambiguity problem in conversion. A low OBS output could mean a low or high SSC, which is challenging to differentiate. Recently, a laser infrared optical sensor was developed by Hohai University (Nanjing, China, HHU-LIOS) with a measurement range up to 30 g/L (Shao and Maa, 2017). This extension of SSC range is a significant improvement, but it is still insufficient for highly turbid environments, e.g., the Yangtze Estuary (Wan et al., 2014) and the Ems Estuary (Winterwerp et al., 2017). A combination of HHU-LIOS and OBS was therefore suggested by Shao and Maa (2017). However, their method only gives SSC at a single point but not a profile.

Acoustic sensors are utilized for measuring SSC profiles non-intrusively, e.g., Acoustic Doppler Profiler (ADP) (Thorne and Hanes, 2002; Ha et al., 2011; Baeye and Fettweis, 2015) and Acoustic Doppler Velocimeter (ADV) (Ha et al., 2009; Salehi and Strom, 2011; Shao and Maa, 2017). In addition to SSC, acoustic sensors also measure flow velocity synchronously. ADP (Moura et al., 2011; Sahin et al., 2013; Fettweis and Baeye, 2015) and ADCP (Guerrero et al., 2011; Anastasiou et al., 2015; Baeye and Fettweis, 2015), for example, concurrently obtain velocity and SSC profiles over several meters. High-frequency acoustic signal (~10 Hz) can be used to estimate turbulent water and sediment flux, e.g., ADV (Fugate and Friedrichs, 2002; Scheu et al., 2015; Yang et al., 2016). Note that optical sensors cannot obtain synchronized high-frequency measurements of velocity at the same location, although they also provide high-frequency SSC estimates (C. Guo et al., 2018; L. Guo et al., 2018). The conversion from acoustic output into SSC has the ambiguity problem and contains significant uncertainties. First, acoustic output increases exponentially with increasing and low SSC (< 1–2 g/L), so a small misalignment in acoustic output may introduce a significant error in its estimate. For instance, 1 dB misalignment in ADV output can cause an error of ~1 g/L in the estimated SSC (Merckelbach and Ridderinkhof, 2006; Shao and Maa, 2017). Second, similar to optical sensors, the acoustic signal also attenuates fast in high SSC (> 1–10 g/L) (Fig. 2, see also Ha et al., 2009; Shao and Maa, 2017), which causes the ambiguity in SSC retrieval.

This study aims to solve the ambiguity problem that a low OBS and ADV reading could mean a low or a high SSC and to access a broader measurement range. We propose an integrated optic and acoustic (IOA) approach to identify the true SSC and obtain high-resolution SSC profile by a combination of OBS, ASM and ADV. This paper is organized in the following way. Section 2 describes the calibration of sensors. Upon careful calibrations, we propose algorithms for each sensor to convert their outputs into SSC in Section 3. Compared with the SSCs from the water samples obtained in the Yangtze Estuary, these algorithms are evaluated. An optimized algorithm is then suggested in Section 4. The accuracy and advantages of the proposed IOA approach are discussed in Section 5. Section 5 also gives a discussion on the observed seasonal SSC profiles and intra-tidal bottom SSC variation in the Yangtze Estuary. It is concluded in Section 6, that the IOA approach is reliable, and it provides wide measurement range up to 300 g/L and high-resolution SSC profiles when the ASM is not saturated. The application of the IOA approach is beneficial for quantifying sediment transport in the bottom boundary layer or highly turbid environments.

2. Sensor calibrations

The OBS (turbidity in NTU) and the ASM (turbidity in FTU) were calibrated in a cylindrical container (0.4 m in diameter and 0.5 m in height) with continuous and steady stirring at the bottom. First, the container was filled with the water collected from the Yangtze Estuary. To determine different SSC level, we gradually poured the slurry (an amalgam of bottom sediment collected every 2 h within a campaign) into the container. The OBS and one of the ASM sensors (88th sensor) were mounted at 15 cm above the bottom with an outlet at the same height for water sampling. At each SSC level, we took a water sample after the turbidity readings stabilized for 30 s. Subsequently, the water sample was filtered through a pre-weighed filter (0.45 μm), and the filter was dried at 40 °C for 48 h to determine the SSC. Averaged turbidity during the sampling was then calibrated against the SSC of water samples (Fig. 1).

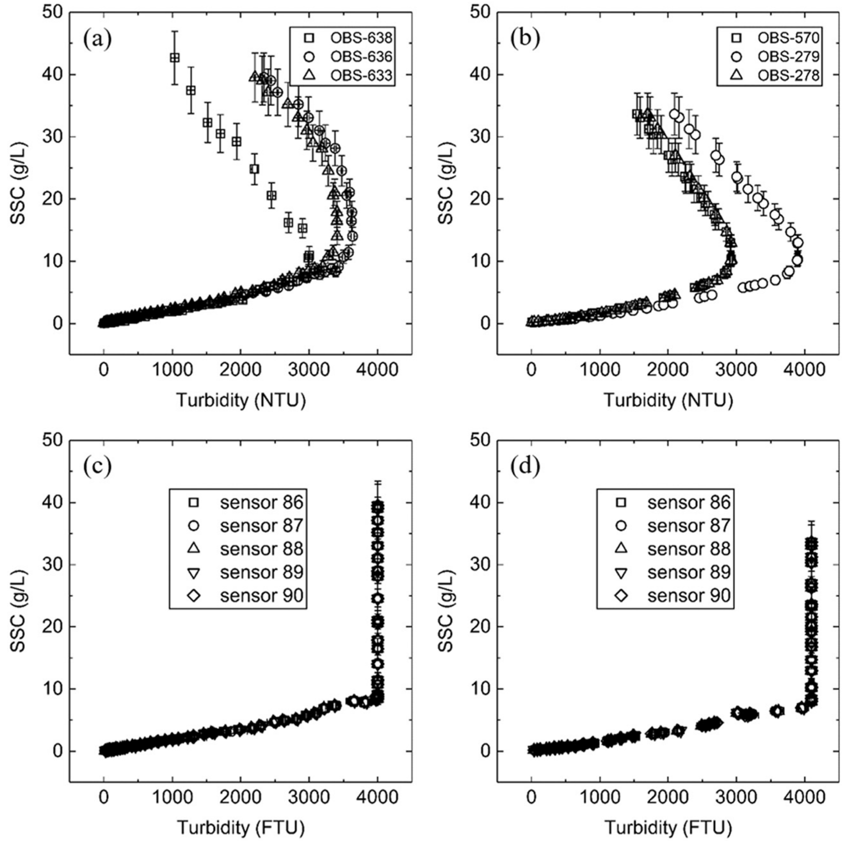

Fig. 1. Calibrations of OBS (turbidity in NTU) (a, b) and ASM (turbidity in FTU) (c, d) against SSC (in g/L) with bottom sediment collected in July 2014 (left panel) and January 2016 (right panel), respectively. Regression results are shown in Table 2.

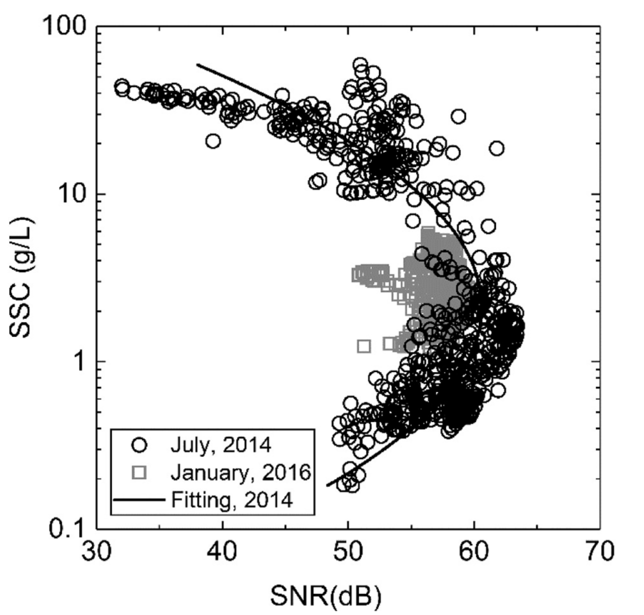

Fig. 2. Calibration of ADV (SNR in dB) against the SSC (in g/L) given by ASM and OBS. Regression results are shown in Table 2.

The calibration of ADV (signal-to-noise ratio, SNR in dB) was carried out with the in-situ SSC derived by ASM and OBS. The sampling rate of the ADV was 8 Hz, and the burst interval was 10 min. In each burst, the ADV sampled continuously for 90 s. In the signal processing, the SNR from three receiving transducers were averaged to obtain the representative mean value, and burst-averaged SNR was then calibrated against the in-situ SSC (Fig. 2).

Calibration results indicate that the response of each sensor (i.e., OBS, ASM and ADV) to increasing SSC is different. ASM turbidity (T_{ASM}) increases linearly with SSC below a limit of ~9 g/L (Fig. 1c and d). Beyond this limit, however, T_{ASM} maintains at the maximum (i.e., saturated). All ASM sensors behave the same (Fig. 1c and d).

The OBS turbidity (T_{OBS}) shows three responses (Fig. 1a and b). At low SSC when T_{ASM} is unsaturated, T_{OBS} increase is approximately linear. A critical OBS turbidity (T_C) can be determined when T_{ASM} just saturates (Fig. 3a). Within a range of moderate SSC, when T_{ASM} saturates and $T_{OBS} \geq T_C$, T_{OBS} remains roughly the same and begins to decrease after reaching the maximum (max T_{OBS}). A parabolic function fits in this range. To relate the turbidity to SSC more directly, we divide the curve into two sections (Fig. 3a, curves 3 and 4). T_{OBS} decreases linearly in high SSC when T_{ASM} saturates and $T_{OBS} < T_C$. Four representative curves are identified to match the transition from one range to the next as continuous as possible (Fig. 3a). Table 2 summarizes the equations of each calibration curve and their correlation coefficients.

The SNR from ADV also has three responses to different SSC level (Fig. 3b), i.e., increasing, constant and decreasing regions. For convenience, parabolic fitting with SSC on a logarithmic scale is applied in this study, and it returns a high coefficient of determination (Table 2). Note that the max SNR occurs in a critical SSC (~2 g/L) (Fig. 2, see also Ha et al., 2009; Shao and Maa, 2017). It means that the SNR decreases monotonically with SSC when ASM is saturated.

3. Conversion algorithms

Based on the different responses of ASM, OBS and ADV, algorithms are developed to convert their outputs into SSC (Fig. 4). To explain the conversion processes, we take the OBS-633, ASM and ADV as examples

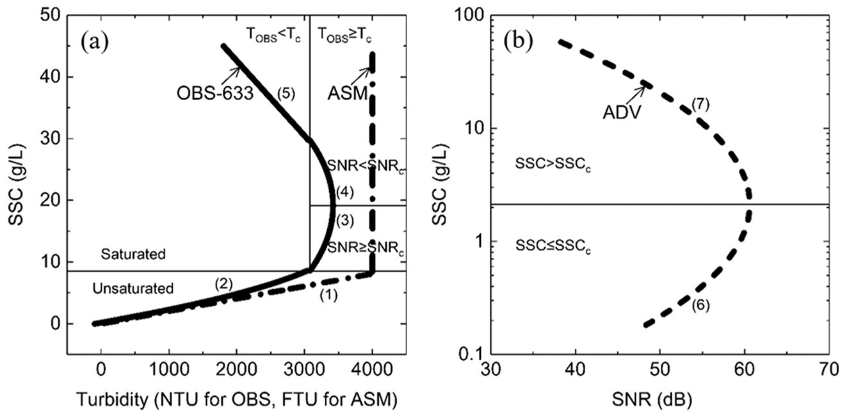

Fig. 3. Examples of calibration curve (ASM, OBS-633 and ADV employed in July 2014) for illustrating the conversion protocols of the IOA approach. T_C denotes the critical OBS turbidity (reading, i.e., $T_C = 3050$ NTU, corresponding to SSC ~ 9 g/L) where ASM just saturates (with a reading around 4000 FTU), and SNR_C (~61 dB) indicates the critical SNR corresponding to the max OBS turbidity (reading, i.e., 3400 NTU, corresponding to SSC = 20 g/L when using OBS). SSC_C indicates the critical SSC (i.e., $SSC_C = 2$ g/L) where the ADV returns the max SNR. The numbers in parenthesis, e.g., (4), is a shorthand of Calibration Relation (CR) 4 as shown in Table 2 and Fig. 4.

(Fig. 3).

The conversion of ASM is relatively simple. Firstly, it needs to identify whether the ASM is saturated or not. The ASM provides estimates only when it is not saturated. Once the ASM saturates, no valid estimate is given. Fortunately, the missing high SSC can be recovered by the OBS or ADV.

The accurate conversion of OBS requires a combined usage of ASM and ADV. Critical OBS turbidity (T_C) and SNR (SNR_C) need to be determined before the conversion (Fig. 3). When the T_{ASM} is not saturated, a second-order polynomial is applied (Fig. 3a, curve 2). For saturated T_{ASM} and $T_{OBS} < T_C$, the estimate is given by a negative and linear relationship (Fig. 3a, curve 5). For saturated T_{ASM} and $T_{OBS} \geq T_C$, the estimate is taken as the smaller solution to the parabolic equation when $SNR \geq SNR_C$ (Fig. 3a, curve 3) and the larger solution when $SNR < SNR_C$ (Fig. 3a, curve 4).

The SSC derived from ASM and OBS serves the conversion of ADV. Upon the determination of critical SSC (SSC_C), the estimate from ADV is taken as the smaller solution to the parabolic equation when $SSC \leq SSC_C$ (Fig. 3b, curve 6) and the larger solution when $SSC > SSC_C$ (Fig. 3b, curve 7).

Table 2
C-R relationship for calibrated sensors. C denotes suspended sediment concentration in g/L, and R represents the readings of OBS (turbidity in NTU), ASM (turbidity in FTU) and ADV (SNR in dB).

Time	Instrument	Conditions	C-R relationship	Number of samples	Correlation index (R^2)
201407	ASM	Unsaturated	$C = 2.0 \times 10^{-3}R$	42	0.99
	OBS-633	Unsaturated	$C = 3.5 \times 10^{-7}R^2 + 1.6 \times 10^{-3}R + 0.2$	42	0.99
		Saturated, $T_{obs} \geq T_c$, $SNR \geq SNR_c$	$C = 19.2 - \frac{\sqrt{41{,}734.0 - 12.2R}}{6.1}$	13	0.92
		Saturated, $T_{obs} \geq T_c$, $SNR < SNR_c$	$C = 19.2 + \frac{\sqrt{41{,}734.0 - 12.2R}}{6.1}$		
		Saturated, $T_{obs} < T_c$	$C = -1.2 \times 10^{-2}R + 66.0$	7	0.97
	OBS-636	Unsaturated	$C = 3.0 \times 10^{-7}R^2 + 1.5 \times 10^{-3}R + 0.2$	42	0.99
		Saturated, $T_{obs} \geq T_c$, $SNR \geq SNR_c$	$C = 18.7 - \frac{\sqrt{42{,}531.8 - 11.7R}}{5.9}$	13	0.93
		Saturated, $T_{obs} \geq T_c$, $SNR < SNR_c$	$C = 18.7 + \frac{\sqrt{42{,}531.8 - 11.7R}}{5.9}$		
		Saturated, $T_{obs} < T_c$	$C = -1.1 \times 10^{-2}R + 65.9$	7	0.97
	OBS-638	Unsaturated	$C = 3.9 \times 10^{-7}R^2 + 1.4 \times 10^{-3}R + 0.1$	34	0.99
		Saturated, $T_{obs} \geq T_c$, $SNR \geq SNR_c$	$C = 10.2 - \frac{\sqrt{104{,}937.2 - 35.0R}}{17.5}$	4	0.98
		Saturated, $T_{obs} \geq T_c$, $SNR < SNR_c$	$C = 10.2 + \frac{\sqrt{104{,}937.2 - 35.0R}}{17.5}$		
		Saturated, $T_{obs} < T_c$	$C = -1.6 \times 10^{-2}R + 59.2$	10	0.97
	ADV	$SSC \leq SSC_c$	$lgC = 0.3 - \frac{\sqrt{2623.2 - 43.3R}}{21.7}$	685	0.70
		$SSC > SSC_c$	$lgC = 0.3 + \frac{\sqrt{2623.2 - 43.3R}}{21.7}$		
201601	ASM	Unsaturated	$C = 1.8 \times 10^{-3}R$	43	0.99
	OBS-278	Unsaturated	$C = 6.9 \times 10^{-7}R^2 + 6.5 \times 10^{-4}R + 0.2$	43	0.99
		Saturated, $T_{obs} \geq T_c$, $SNR \geq SNR_c$	$C = 11.5 - \frac{\sqrt{80{,}551.5 - 27.5R}}{13.7}$	9	0.99
		Saturated, $T_{obs} \geq T_c$, $SNR < SNR_c$	$C = 11.5 + \frac{\sqrt{80{,}551.5 - 27.5R}}{13.7}$		
		Saturated, $T_{obs} < T_c$	$C = -1.6 \times 10^{-2}R + 61.1$	14	0.99
	OBS-279	Unsaturated	$C = 3.2 \times 10^{-7}R^2 + 8.2 \times 10^{-4}R + 0.2$	43	0.99
		Saturated, $T_{obs} \geq T_c$, $SNR \geq SNR_c$	$C = 11.6 - \frac{\sqrt{176{,}062.0 - 45.0R}}{22.5}$	9	0.99
		Saturated, $T_{obs} \geq T_c$, $SNR < SNR_c$	$C = 11.6 + \frac{\sqrt{176{,}062.0 - 45.0R}}{22.5}$		
		Saturated, $T_{obs} < T_c$	$C = -1.1 \times 10^{-2}R + 57.0$	14	0.99
	OBS-570	Unsaturated	$C = 6.0 \times 10^{-7}R^2 + 9.1 \times 10^{-4}R + 0.2$	43	0.99
		Saturated, $T_{obs} \geq T_c$, $SNR \geq SNR_c$	$C = 11.4 - \frac{\sqrt{81{,}988.4 - 28.0R}}{14.0}$	9	0.99
		Saturated, $T_{obs} \geq T_c$, $SNR < SNR_c$	$C = 11.4 + \frac{\sqrt{81{,}988.4 - 28.0R}}{14.0}$		
		Saturated, $T_{obs} < T_c$	$C = -1.5 \times 10^{-2}R + 56.1$	14	0.99

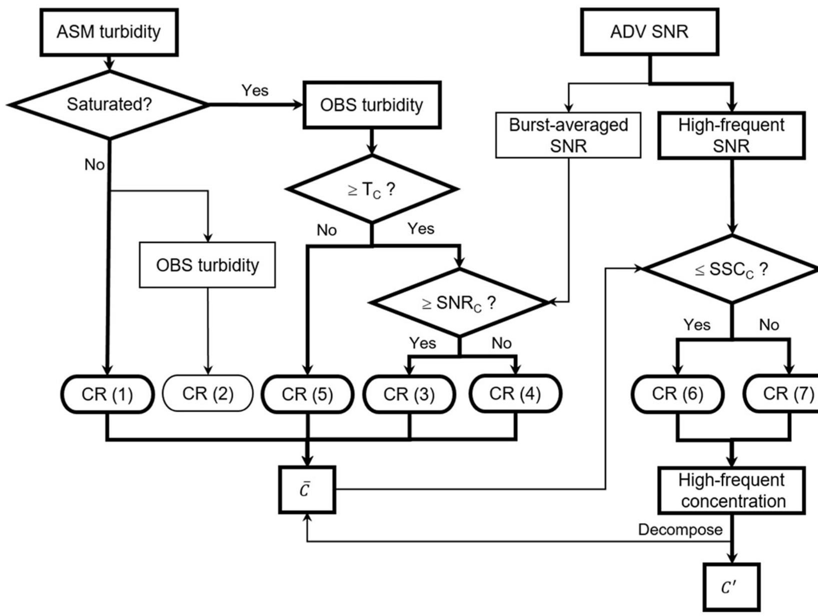

Fig. 4. Algorithms for ASM, OBS and ADV to estimate reliable SSC. CR denotes the calibration relationship between suspended sediment concentrations and readings of sensors (i.e., turbidity and SNR) given in Table 2. Highlighted flowcharts show the optimal protocol according to the performance of each sensor.

4. Application and evaluation

To test and evaluate the proposed IOA approach and algorithms, we conducted field campaigns in July 2014 (wet season) and January 2016 (dry season), respectively, in the turbidity maximum zone of the Yangtze Estuary. The mean river discharge was 44,350 m^3/s and 21,200 m^3/s in the wet and dry season, respectively. Upon the calibrations between the SSC given by the optical and acoustic sensors and water sampling, an optimized algorithm is suggested. We will also show measured SSC profiles with and without such an algorithm, highlighting the effectiveness and advantage of the IOA approach.

4.1. Field campaigns in the Yangtze Estuary

The Yangtze Estuary is an excellent example of highly turbid water, particularly in its estuarine turbidity maximum (ETM) where the SSC is > 10 g/L near the bottom (He et al., 2001; Shi et al., 2006; Wan et al., 2014). Two campaigns were conducted in the North Passage (Fig. 5). For each campaign, both tripod- and ship-borne systems with multiple sensors were employed. Table 3 summarizes the operated instruments and their sampling schemes.

A sketch of the bottom-mounted tripod system is given in Fig. 5d. An ASM measured turbidity profiles from 0.11 to 1.06 m above the bed (mab here-after). An OBS simultaneously measured turbidity, salinity, and temperature at 0.35, 0.55 and 1.06 mab, respectively. A downward-looking ADV recorded high-frequency 3D velocities and SNR at 0.35 mab. The sensors in the ADV were also used to monitor the heading, pitch and roll state of the tripod.

Ship-borne observations included measurements of turbidity, salinity and velocity profiles, and water sampling. Turbidity and salinity profiles were hourly measured by the OBS moved from water surface to near-bed (~0.5 m). The OBS stayed for 30 s at each of six depth layers, i.e., 0.05 (near-surface), 0.2, 0.4, 0.6, 0.8, and 0.95 (near-bed) of the water depth. A water sample of 1.2 L was concurrently collected at each layer. These water samples were used for laboratory analysis of SSC, salinity and primary particle size distribution. The particle size was measured by a Coulter Counter analyzer after removing organic material and destroying flocs by sonification. An LISST-100C hourly recorded the in-situ floc size distribution and volume concentration at each layer. Bottom sediment was collected every 2 h for the calibration of tripod-borne sensors.

To avoid interference between tripod- and ship-borne sensors, the tripod was deployed about 200 m upstream of the vessel. Compared with the distance between the two groins (~5 km), this distance is negligible. For safety reasons, it is not allowed to deploy an instrument tripod or mooring vessel in the Deepwater Navigational Channel (DNC). In our cases, both tripod- and ship-borne measurements were conducted at the south part of the channel, about 200 m away from the DNC (Fig. 5c). Due to significant differences in cross-channel hydrodynamics and topography (Song et al., 2013; Wan et al., 2014; Ge et al., 2015), the tripod and the vessel should keep the same distance from the DNC. Then we can assume that the tripod- and ship-borne measurements are representative for the same site, although they are actually in different locations.

The temporal and spatial variations of water temperature were small within a campaign, e.g., 24.7–27.0 °C in July 2014 and 3.5–6.1 °C January 2016. Hence the impact of temperature on the sensors was negligible. The water temperature difference between the two campaigns, however, was significant, so we respectively calibrated the sensors at the temperature similar to the on-site water temperature.

4.2. SSC from in-situ water samples

To evaluate the performance of each sensor, we take the SSC from in-situ water sampling as the reference. The water depth (H) ranged from 9 to 13 m (Figs. 6a and 7a), so the bottom SSC (at 0.95H) represented the SSC at 0.45–0.65 mab which can be used for the evaluation of tripod sensors. The SSC from water samples can only be verified by comparing samples that were taken close to each other and at the same time. Unfortunately, such samples were not available in our study. Note that the SSC may be incorrect due to sampling and analysis errors. However, we do not have direct indications.

The SSC ranged 0.4–39.8 g/L during the campaign in July 2014 (Fig. 6c) and 1.4–5.1 g/L in January 2016 (Fig. 7c). High SSC values and a wide SSC range in July 2014 are preferred to evaluate the performance of the IOA approach. Concerning intra-tidal variation (Figs. 6c and 7c), the SSC increased after low water slack (LWS). The SSC peaked around the max flood, and decreased slightly thereafter. After high water slack (HWS), the SSC increased rapidly again, reaching another peak on the early ebb. Subsequently, the SSC dropped and

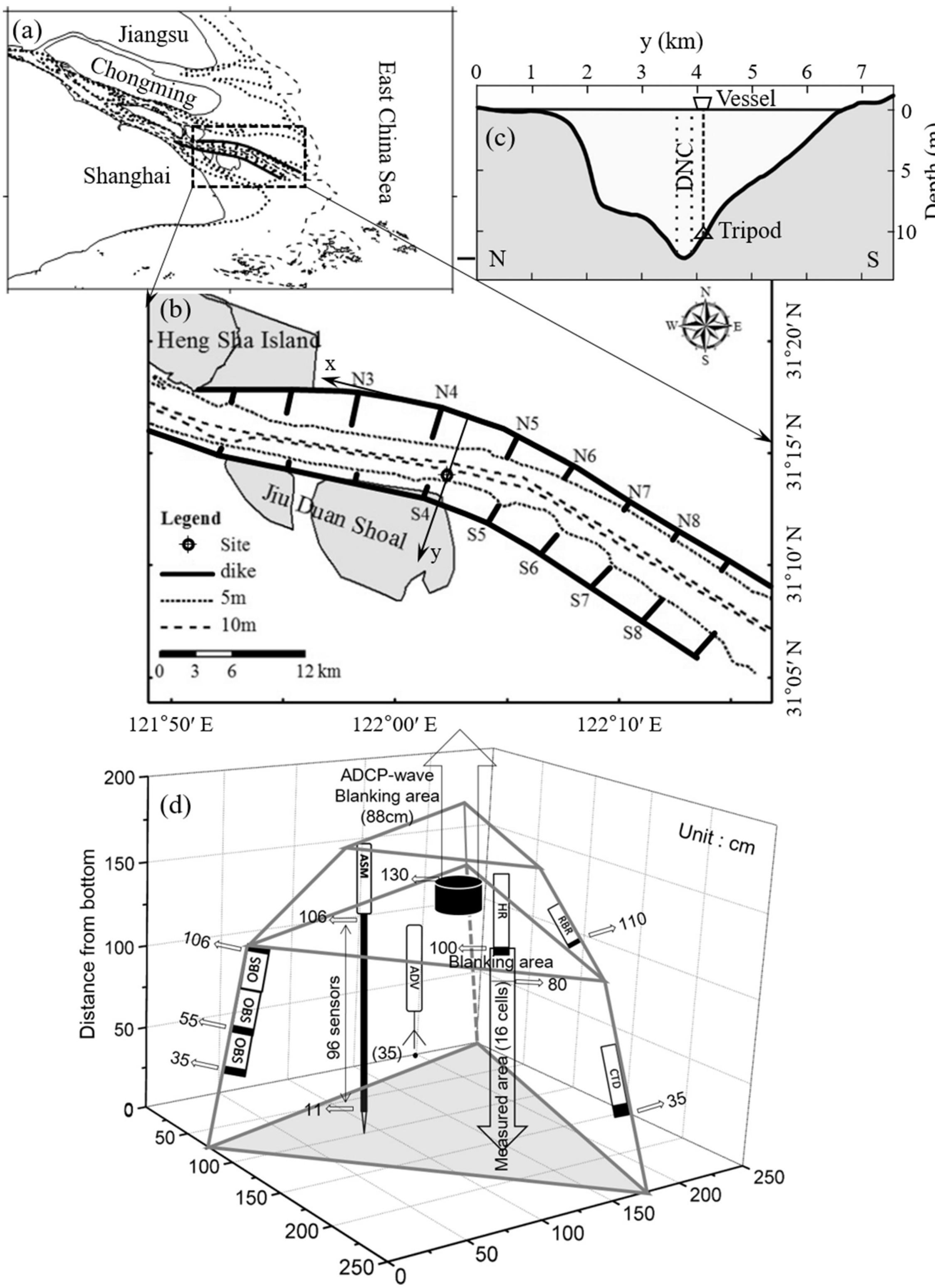

Fig. 5. The Yangtze Estuary (a), the Deepwater Navigational Channel (DNC) at the North Passage (b), the positions of the DNC and the moored tripod and shipboard observation systems in an estuarine cross section (c), and the schematic of bottom-mounted tripod system with multiple sensors (d). The numbers in (d) represent the distance of the sensor above the seabed.

reached the minimum at LWS. Similar intra-tidal variation pattern occurred in January 2016, except the higher SSC in the wet season and postponed peak in the late flood of the dry season.

The SSC from the water sample was > 10 g/L at 15:00–17:00 on July 14, 2014 (Fig. 6c). During this period, the ASM was saturated, and both the OBS and ADV outputs decreased significantly. It suggests that the observed high SSCs were consistent, and they caused optical and acoustic attenuation in the field. The SSC, however, decreased suddenly to ~1 g/L at 2:00–5:00 on July 15, when the ASM was saturated. Meanwhile, the bottom turbidity was > 3000 NTU, which can be validated by both tripod- and ship-borne OBS, indicating an SSC > 10 g/L. There are chances that the SSC from water sampling is

Table 3
Shipboard and tripod instruments and their sampling schemes.

Carrier	Instrument deployed	Distance above bed (mab)	Sampling interval (min)	Sampling duration (s)	Sampling frequency (Hz)	Survey parameter	Profile resolution (m)
Vessel	ADCP	> 1.5	Continuously	Continuously	0.1	Upper velocity	0.5
	OBS	> 1.0	60	30	1	SSC, salinity, temperature	0.1
	LISST	[a]	60	30	1	FSD	–
	Water sampler	[a]	60	30	–	SSC, salinity, PPSD	–
Tripod	ACP	< 0.8	5	60	1	Near-bed velocity	0.05
	ADCP-wave	> 2.0	5	60	1	Upper velocity, wave	0.5
	RBR	1.1	5	60	1	Wave	–
	ADV	0.35	10	90	8	Near-bed velocity, SSC	–
	ASM	0.11–1.06	5	60	1	SSC	0.01
	OBS	0.35, 0.55, 1.06	5	60	1	SSC, salinity, temperature	–

[a] Data or samples collected at six relative depth layers, i.e., 0.05H (near surface), 0.2H, 0.4H, 0.6H, 0.8H, and 0.95H (near-bed), where H is the total water depth. FSD and PPSD denote the flocculate and primary particle size distribution, respectively.

underestimated during this period. This underestimation could be the result of sampling not close enough to the bed, and/or error of analysis in the laboratory. The underestimated SSC (only one sample) was therefore excluded in the evaluation.

4.3. SSCs from OBS, ASM and ADV

The T_{ASM} saturated (with a reading around 4000 FTU) on the early ebb, which suggests a high SSC > ~9 g/L in July 2014. Meanwhile, a significant reduction in T_{OBS} and SNR occurred. Such responses of T_{ASM}, T_{OBS} and SNR to high SSC can be reproduced in the laboratory experiments (Figs. 1 and 2). It indicates that the response of each sensor is stable and reliable in the lab a well as in the field.

Figs. 6c (July 2014) and 7c (January 2016) show the time series of ASM-, OBS- and ADV-derived SSC at 0.35 mab. All SSCs given by sensors follow similar intra-tidal variation as the water sampling results.

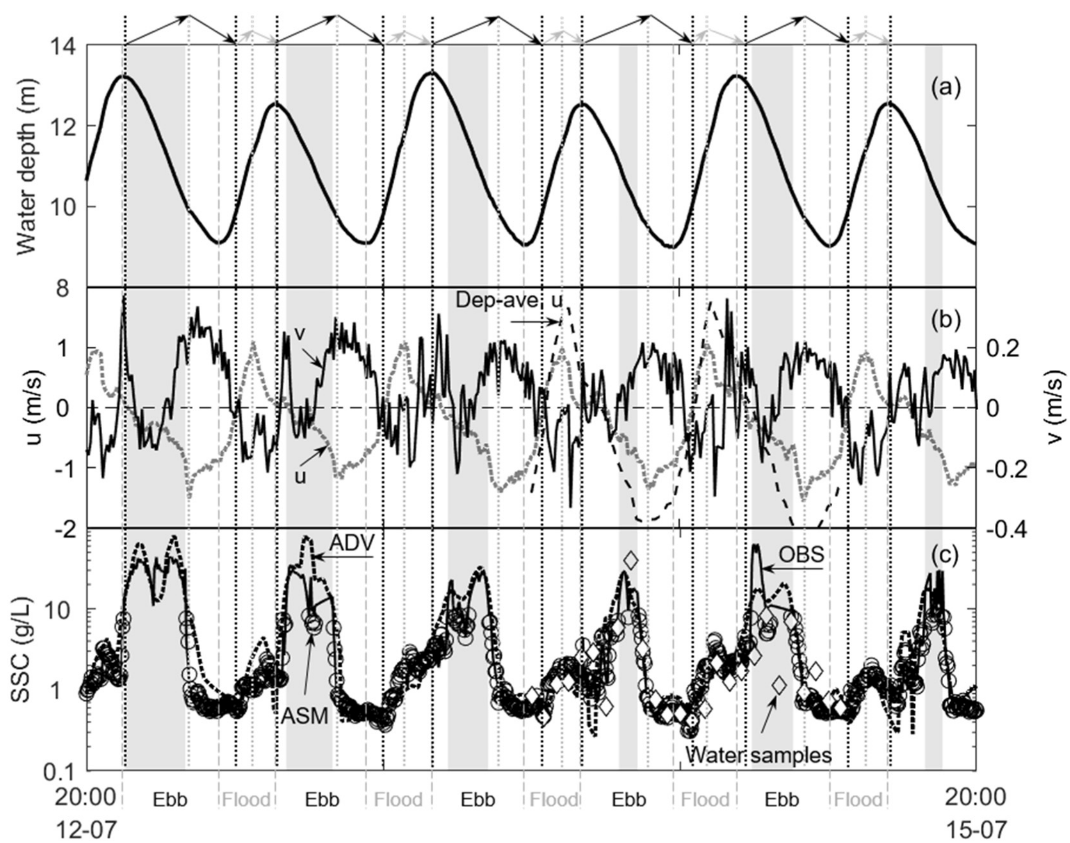

Fig. 6. Time series of 2014 July (wet season) measurements in the North Passage, Yangtze Estuary. (a) water depth measured by the CTD, (b) along- (u, grey dot) and cross- (v, black solid) channel velocity measured by the ADV at 0.35 m above bed (mab) and depth-averaged u (black dash); (c) SSCs from the filtration of water samples collected at the bottom layer (i.e., 0.95H, diamond), and ASM (circle), OBS (solid line) and ADV (dot line) at 0.35 mab. Note that the estimates given by the ASM are missing when it is saturated. Positive u indicates the flood direction, and positive v represents the cross-channel velocity from the north to the south. Since the survey site locates at the south to the channel, positive v also indicates the channel-to-shoal flow. The time period for flood (grey) and ebb (black) are marked at the bottom. The tidal current acceleration phases are marked on top by arrows with a positive slope, and the deceleration phases are marked by arrows with a negative slope. The shadow area indicate the periods when SSC > 10 g/L. The tidal current phase between near-bed and depth-averaged velocity is roughly the same.

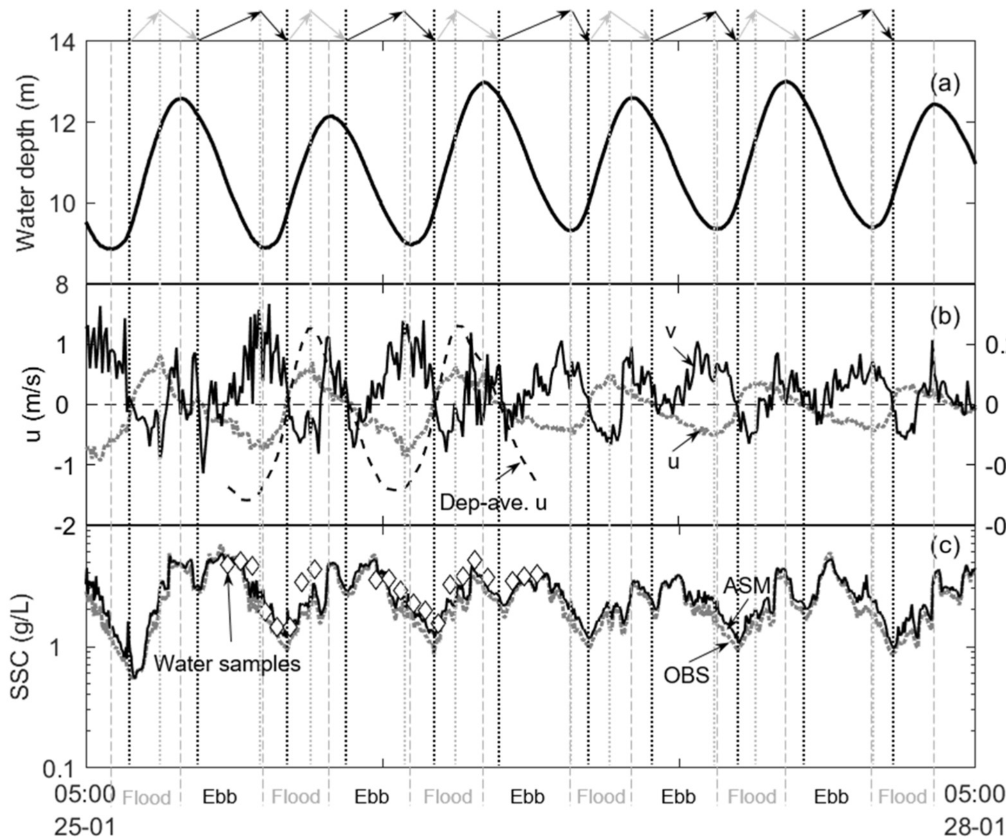

Fig. 7. Time series of 2016 January (dry season) measurements in the North Passage, Yangtze Estuary. (a) water depth measured by the CTD, (b) along- (u, grey dot) and cross- (v, black solid) channel velocity measured by the ADV at 0.35 m above bed (mab) and depth-averaged u (black dash); (c) SSCs from the filtration of water samples collected at the bottom layer (i.e., 0.95H, diamond), and ASM (solid line) and OBS (grey dot line) at 0.35 mab. Positive u indicates the flood direction, and positive v represents the cross-channel velocity from the north to the south. Since the survey site locates at the south to the channel, positive v also indicates the channel-to-shoal flow. The time period for flood (grey) and ebb (black) are marked at the bottom. The tidal current acceleration phases are marked on top by arrows with a positive slope, and the deceleration phases are marked by arrows with a negative slope. The tidal current phase between near-bed and depth-averaged velocity is roughly the same.

The OBS and ADV output higher SSC (> 60 g/L), while the ASM only provides reliable estimates < 9 g/L.

The ADV also provides estimates of turbulent sediment flux ($\overline{w'c'}$). The observed $\overline{w'c'}$ had a tidally averaged magnitude of 10^{-4} kg/m^2/s and reasonable intra-tidal variation, similar to the theoretical calculations ($\frac{\upsilon_t}{\sigma_t}\frac{\partial c}{\partial z}$) (Fig. 8). υ_t is the eddy viscosity given by

$$\upsilon_t = \left(\overline{u'w'}\frac{\partial \overline{u}}{\partial z} + \overline{v'w'}\frac{\partial \overline{v}}{\partial z}\right)\left[\left(\frac{\partial \overline{u}}{\partial z}\right)^2 + \left(\frac{\partial \overline{v}}{\partial z}\right)^2\right]^{-1} \tag{1}$$

where σ_t is the turbulent Prandtl–Schmidt number, relating eddy viscosity (υ_t) to eddy diffusivity (K_t), as $K_t = \upsilon_t / \sigma_t$. A common assumption is that $\sigma_t = 0.7$. In highly turbid environments (e.g., the Yangtze Estuary), however, $\sigma_t = 2.0$ gives the optimal modeling of currents and SSC (Winterwerp et al., 2009). Direct comparison between the calculations ($\frac{\upsilon_t}{\sigma_t}\frac{\partial c}{\partial z}$) and in-situ measurements ($\overline{w'c'}$), verifies that $\sigma_t = 2.0$ gives a better estimate than $\sigma_t = 0.7$ (Fig. 8).

4.4. Optimal algorithm in the IOA approach

The performance of each sensor is evaluated by an averaged relative

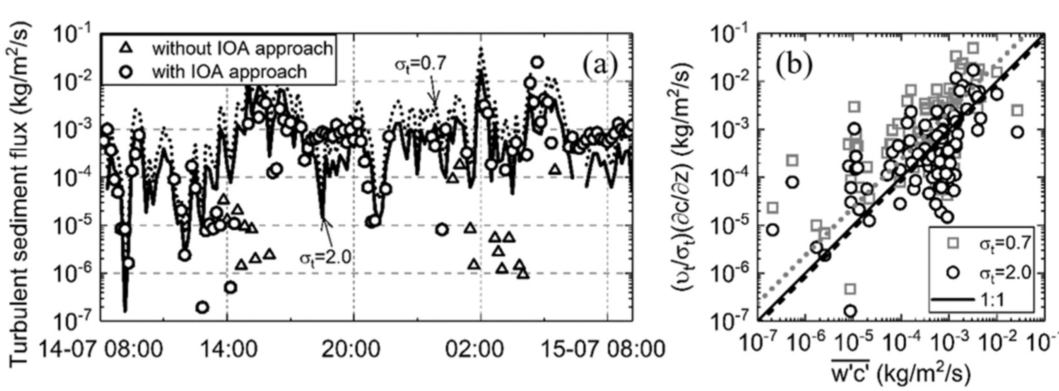

Fig. 8. Comparison between ADV-derived turbulent sediment flux ($\overline{w'c'}$) and the theoretical calculations ($\frac{\upsilon_t}{\sigma_t}\frac{\partial c}{\partial z}$) with two classic values of turbulent Prandtl–Schmidt number, i.e., $\sigma_t = 0.7$ and $\sigma_t = 2.0$. ADV-derived $\overline{w'c'}$ with and without the proposed algorithm are also presented (a).

Table 4
Measurement ranges (g/L) of ASM, OBS and ADV with their relative errors (%). Missing values are represented by the symbol NA (Not Available).

Time	Instrument	Range (g/L)	Relative error (%)
201407	ASM	0.0–8.0	33.6
	OBS-633	0.2–66.0	32.2
	OBS-636	0.2–65.9	NA
	OBS-638	0.1–59.2	NA
	ADV	0.1–457.3	88.6
201601	ASM	0.0–7.4	17.6
	OBS-278	0.2–61.1	28.2
	OBS-279	0.2–57.0	NA
	OBS-570	0.2–56.1	NA

error:

$$Relative\ error = \frac{\overline{|C_{calculated} - C_{observed}|}}{\overline{C_{observed}}} \times 100\% \tag{2}$$

where $C_{calculated}$ is the SSC estimated by sensors; $C_{observed}$ denotes to the SSC from the filtration of water sample (Druine et al., 2018).

Table 4 summarizes the relative error and measurement range of each sensor. ASM-derived SSC contains the lowest relative error (~25%), although it has a limited measurement range (< 9 g/L). The ASM also provides high-resolution SSC profiles when it is not saturated. Our proposed algorithms successfully extend the measurement range of OBS to ~60 g/L, and OBS-derived SSC has a relative error of about 30%. Although the ADV has the most extended measurement range (~360 g/L), its estimates contain the largest uncertainty (relative error > 80%), so the best it can be used is to have a rough estimation and assist in the conversion of OBS. According to the sensor performances, we suggest an optimized algorithm for the IOA approach (Fig. 4). The ASM-derived SSC is preferred as long as the ASM is unsaturated. Under ASM-saturated condition, the missing high SSC can be recovered by the OBS. The ADV can provide a rough estimation of the trend and reduce the uncertainty in the OBS conversion.

4.5. Performance of the IOA approach

Fig. 9 shows the estimated SSC profiles, which highlights the advantages of the IOA approach. According to the conventional method (i.e., without IOA approach), the SSC is estimated by only OBSs at three layers (i.e., 0.35, 0.55 and 1.06 mab), in which case the high-SSC-induced attenuation cannot be identified. Only the results below the saturation point are reliable (e.g., curve 2 in Fig. 3), which may underestimate high SSCs.

When the SSC is low, i.e., < 10 g/L, the two methods (with and without IOA approach) give similar SSC estimates (Fig. 9a), other than significant differences near the bed (Fig. 9b and c). The SSC can be significantly underestimated, and it was generally smaller than 10 g/L without the IOA approach when it was actually up to 63 g/L.

The ASM confirms the OBS results and provides high-resolution SSC profiles (Fig. 9d, e and f). Ninety-six estimates are given in a profile with a vertical resolution of 1 cm. Without the IOA approach, however, only three estimates are given by the OBSs. When the near-bed high SSC appears, the IOA approach provides a more reasonable and reliable SSC profile. At 01:40 am, July 12 (Fig. 9d), for example, the proposed IOA approach outputted an SSC of ~40 g/L at 0.35 mab, while an SSC of ~4 g/L was obtained without the IOA approach. The ASM results show a sudden increase in SSC at 0.55 mab, which suggests that the SSC profile estimated by the IOA approach is more reasonable.

The IOA approach with the optimized algorithm allows high temporal and vertical resolution of SSC variability. Particularly on the early ebb in July 2014, the concentrated benthic suspension (CBS) was successfully captured and measured. The observed CBS persisted 3–4 h, with a thickness was ~1 m (Fig. 10c). In the wet season (Fig. 12a), the SSC profile was L-shaped with a much higher bottom SSC (up to 63 g/L). A significant SSC gradient was present in the lowest 0.2H. In the dry season (Fig. 12e), however, the SSC profile was more uniform. The SSC showed the highest value just above the bed and decreased almost linearly to the surface.

5. Discussion

5.1. Sources of uncertainties

Although with improvement, the sensors and the obtained SSCs are somehow imbedded with uncertainties and bias. The OBS and ASM turbidity, for example, have an uncertainty of ± 10% (Argus, 2014; Campbell Scientific, 2018). Since a linear regression is applied for the ASM calibration, this uncertainty will cause a relative error of 10% in ASM-derived SSC. As regards the OBS, this uncertainty also leads to a relative error of 10% in the linearly increasing and decreasing region (i.e., curves 2 and 5 in Fig. 3a), but up to 90% around the turning point (i.e., curves 3 and 4 in Fig. 3a). Since the SNR is calibrated against the SSC on a logarithmic scale, the relative error caused by the SNR uncertainty therefore increases with increasing SSC. Near the turning point (SSC = 2 g/L), for example, a SNR uncertainty of ± 1% (Nortek, 2005) causes a relative error of 30%. The relative errors in Table 4, however, are higher than those caused by the uncertainty of raw signal, which suggests additional sources for the given relative errors.

In this study, the sensors were evaluated by water samples in the bottom layer (0.95H, i.e., ~0.45–0.65 mab), while the sensors were deployed at 0.35 mab. Such a height difference may enlarge the estimated relative error, particularly when a large near-bed SSC gradient presents (e.g., July 2014). Besides, the ADV was calibrated by the OBS- or ASM-derived SSC. The uncertainty and bias of ADV-derived SSC, therefore, may accumulate from those of the OBS or ASM. In other words, the relative error of ADV-derived SSC is also overestimated.

Since the grain size and composition of suspended sediment can affect the responses of both optical and acoustic sensor (Conner and De Visser, 1992; Gibbs and Wolanski, 1992; Green and Boon, 1993; Merten et al., 2014; Su et al., 2016; Druine et al., 2018), tidal variation of grain size or sediment composition could also introduce errors to the SSC estimates. In the Yangtze Estuary, size and density of flocculates continuously change in response to the complex advection, resuspension, deposition and flocculation processes (Guo et al., 2017). During the campaign in July 2014, the median grain size of primary particles (D_{P50}) ranged 4–20 μm, with an average of ~10 μm. The primary sediment particles were larger in size in January 2016 (Table 5). The content of clay, silt and sand varied largely over time and in depth (Fig. 13 and Table 5). In July 2014, for example, both floc size (15–90 μm) and density (80–800 kg/m^3) had a broad range. Such strong variations in grain size and floc density could be one of the sources for the relative error of SSC estimates.

In sensor calibrations, we reduce the effects of particle size by using the mixture of bottom sediment collected every 2 h during the campaign. To a certain extent, this mixture represents the tidally averaged condition of suspended sediment in the bottom layer (Fig. 13). The calibration thus returns a representative curve for a tide-averaged condition. Upon these calibrations, the proposed IOA approach gives SSC estimates with a relative error of 17–34%. This error is acceptable for in-situ SSC measurement and the quantification of sediment transport.

5.2. Advantages and disadvantages of the IOA approach

By the IOA approach, both OBS and ADV access a broader measurement range of SSC (Table 4), as the ambiguity problem in conversion is solved. Upon calibration in high SSC, the OBS can provide estimates even up to 300 g/L (Kineke and Sternberg, 1992). Although the ADV also has an extended measurement range (> 300 g/L), the best

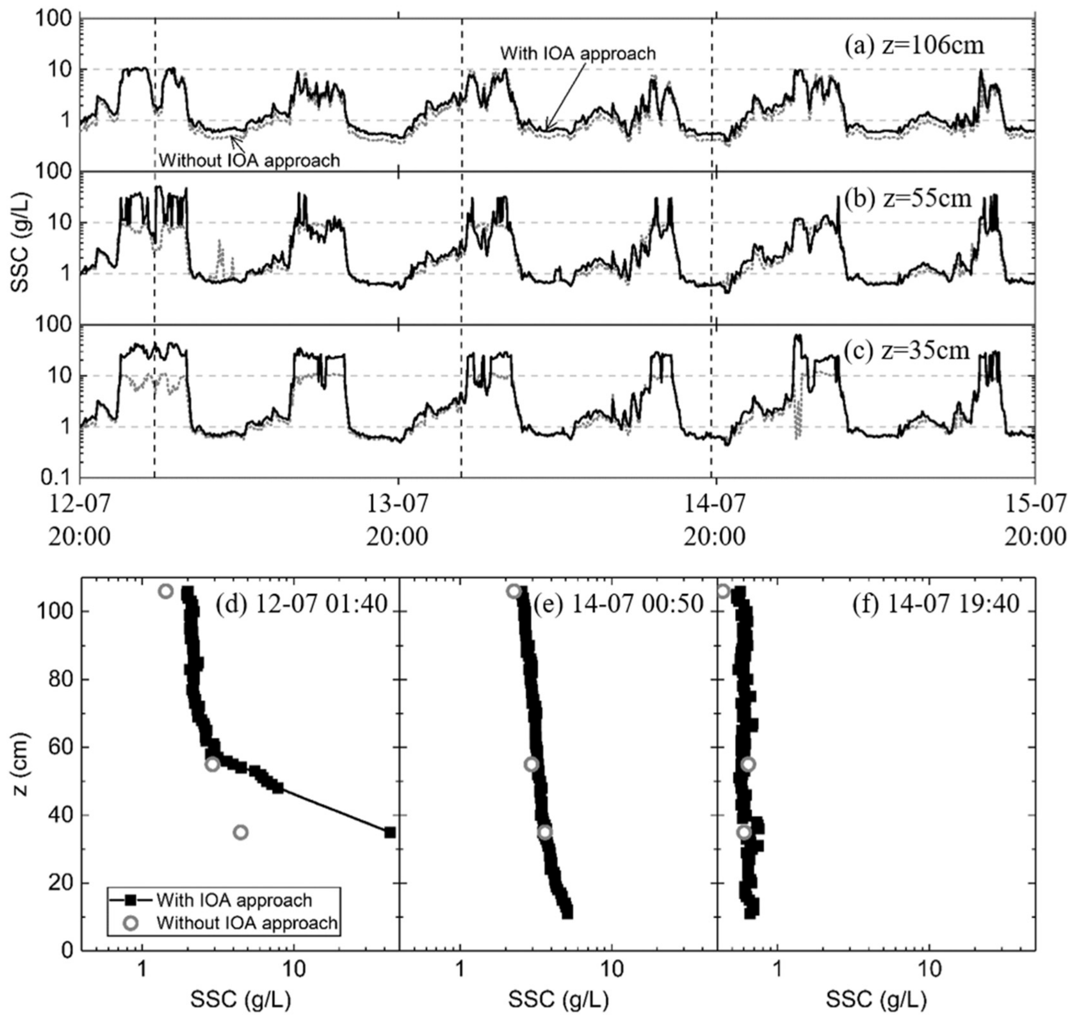

Fig. 9. Time series of SSC from three tripod mounted OBSs with (black solid) and without (grey dot) the IOA approach at 106 cm (a), 55 cm (b) and 35 cm (c) above bed, and three representative SSC profiles within high (d), mid (e) and low (f) SSC. The ASM readings below 50 cm from bed are saturated (d), and thus, removed, except the one at 35 cm above bed, which was recovered by the OBS reading at that time. A straight line between the SSCs from ASM at 35 and 50 cm is suggested as the possible SSC profile.

way it can be used is to give a rough estimation and to assist in OBS conversion, because of the large uncertainty of its estimates. With the IOA approach, we successfully captured and measured the CBS (SSC > 10 g/L) in the Yangtze Estuary.

The IOA approach also provides high-resolution SSC profiles by the ASM. In this study, the ASM was deployed on a tripod and measured the SSC profiles in the bottom boundary layer. These profiles have a higher resolution (0.01 m) than those measured by acoustic sensors (0.25–1.0 m), e.g., ADCP (Anastasiou et al., 2015; Baeye and Fettweis, 2015) and ADP (Fettweis and Baeye, 2015). Note that the ASM can produce valid high-resolution SSC profile only when it is not saturated. Once the ASM sensor is saturated, the estimate given by ASM is missing. These missing values, however, can be recovered by the OBS.

The IOA approach also provides direct and reliable measurements of turbulent sediment flux ($\overline{w'c'}$) by the ADV. Unlike optical sensors, the ADV provides estimates of turbulent velocity (w') and SSC (c') directly at the same position. Fig. 8 shows the ADV-derived $\overline{w'c'}$ with and without the IOA approach, as well as the theoretical calculations with σ_t = 0.7 and 2.0. Without the IOA approach, the $\overline{w'c'}$ is significantly underestimated (Fig. 8a). The $\overline{w'c'}$ with the IOA approach, however, maintains close to the theoretical calculation with σ_t = 2.0, which is consistent to the observations by Cellino and Graf (1999) and modeling results by Winterwerp et al. (2009) in highly turbid water.

The IOA approach and the optimized algorithm, however, are not perfect. First, sensor responses to SSC are not entirely the same between the field and laboratory experiments. The OBS, for example, had a small amount (< 1%) of outputs during the field campaign that exceeded the maximum turbidity (~3400 NTU) obtained in the in-lab calibration experiment. Part of the SSC given by the IOA approach is therefore missing. Maa et al. (1992) suggested that both clay mineralogy and salinity affect the OBS response to SSC. In our study, sediment samples used in the calibration were collected from the bed surface at the survey site. Their clay mineralogy thus did not change too much compared with the near-bed suspensions (Fig. 13). The salinity, however, ranged 0–12‰ during the field measurement in July 2014, whereas the mixture of water samples returned a representative mean salinity of 5‰ in the in-lab calibration. Therefore, the salinity of ambient water is likely the main reason for the difference between the in-lab and in-filed response of an OBS, and in-situ calibration is recommended. Second, the effects of particle size are not taken into account in the proposed algorithm. To further improve the accuracy, careful calibrations with the particle size correction (Green and Boon, 1993; Su et al., 2016) are suggested in future application.

5.3. Seasonal SSC profiles

The two studying periods (wet and dry seasons) show very different vertical SSC profiles (Fig. 12a and d). In the wet season, the SSC is

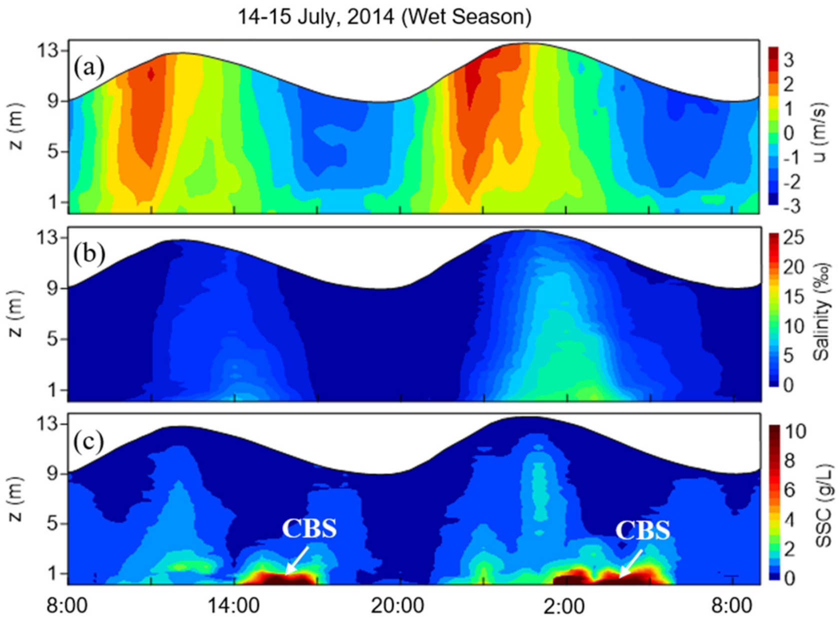

Fig. 10. Time-depth variability of (a) along-channel velocity (u), (b) salinity and (c) SSC during 14–15 July 2014. Positive u indicates the flood direction. CBS denotes the concentrated benthic suspension (SSC > 10 g/L).

higher in the benthic layer, but lower higher up in the water column; in the dry season, the opposite is found. Such a seasonality may correlate with the seasonal location of salinity wedge and ETM, estuarine stratification, floc size and settling velocity.

In the dry season, both the salinity wedge (Figs. 11b and 12f) and ETM (Wan, 2015; Figs. 7–12) locate further upstream, and thus the lower half of the water column may have a more uniform SSC profile, because of the thick salinity wedge and better mixing capability, especially the lowest 0.2H (Fig. 12e). In the wet season, the wedge moves downstream; and only its head can reach the survey station (Figs. 10b and 12b). The observed wedge is therefore relatively thin, and the near-bed mixing is weak. As a result, the vertical SSC gradient is high near the bed. The thickness of this wedge is > 2 m so that a high SSC gradient was observed at the experimental site. In other words, the near-bed SSC in the channel could be higher than that observed at the survey station.

In addition to wedge and ETM movement, the increasing freshwater discharge also enhances the strain-induced stratification (Simpson et al., 1990) and therefore estuarine circulation (Wan, 2015). The enhanced stratification benefits sediment trapping near the bottom (Geyer, 1993), while the circulation accumulates sediment in the convergent zone (i.e., ETM). As an overall result, both the SSC and its gradient are high near the bottom in the wet season. Although a stronger residual current (Fig. 12c and g) occurs in the wet season, depth-integrated sediment flux (Fig. 12d and h) is roughly the same. Because of the increasing sediment supply from the upstream (C. Guo et al., 2018; L. Guo et al., 2018), sediment accumulation therefore accelerates in the wet season, reaching a higher SSC.

The seasonality of SSC profile may also be the result of the changes in floc size and settling velocity. Both floc size and settling velocity are large in the wet season, and thus the suspension is more concentrated in the near-bed layer, because of the low turbulent shear (Wu et al., 2012) and high chlorophyll concentration (Fettweis and Baeye, 2015; Deng et al., 2019); and vice versa in the dry season. The quantification of the above processes, however, is waiting for detailed flocs, turbulence, and ETM data.

Table 5
Tidally averaged median grain sizes of primary particles (D_{P50}) and flocculates (D_{F50}), dry density of flocculates ($\rho = \bar{c}/V_c$, where $\bar{c}$ is the sediment concentration of water sample and V_c is the volume concentration measured by LISST) and composition of suspended sediment in different layers with their standard deviations. Data are not available in the bottom layer as LISST does not work correctly in high turbidity. Missing values are represented by the symbol NA (Not Available).

Time [yymm]	Position	D_{P50} (std.) [μm]	D_{F50} (std.) [μm]	ρ (std.) [kg/m^3]	P_{clay} (std.) [%]	P_{silt} (std.) [%]	P_{sand} (std.) [%]
1407	0.05H	6.0 (± 1.4)	26.3 (± 8.8)	310 (± 84)	39 (± 6)	56 (± 8)	5 (± 6)
	0.2H	7.3 (± 2.1)	24.7 (± 7.4)	311 (± 91)	35 (± 6)	61 (± 7)	4 (± 4)
	0.4H	8.9 (± 3.3)	25.7 (± 10.7)	304 (± 130)	32 (± 6)	64 (± 4)	4 (± 4)
	0.6H	10.4 (± 4.0)	27.5 (± 16.3)	275 (± 82)	30 (± 5)	65 (± 3)	5 (± 5)
	0.8H	11.6 (± 4.2)	33.9 (± 19.5)	238 (± 78)	28 (± 5)	66 (± 2)	6 (± 5)
	0.95H	13.5 (± 6.0)	33.3 (± 6.3)	246 (± 42)	27 (± 6)	63 (± 3)	10 (± 7)
	Bed	12.1 (± 2.7)	NA	NA	27 (± 3)	64 (± 5)	9 (± 3)
	All samples	9.8 (± 4.5)	27.6 (± 12.8)	288 (± 97)	32 (± 7)	62 (± 6)	6 (± 5)
1601	0.05H	9.4 (± 4.0)	23.7 (± 5.4)	502 (± 339)	31 (± 7)	66 (± 6)	2 (± 2)
	0.2H	12.6 (± 5.8)	NA	NA	27 (± 6)	69 (± 4)	4 (± 3)
	0.4H	14.6 (± 5.2)	NA	NA	25 (± 5)	71 (± 3)	4 (± 3)
	0.6H	16.2 (± 5.0)	NA	NA	22 (± 4)	72 (± 2)	6 (± 4)
	0.8H	18.6 (± 5.4)	NA	NA	21 (± 4)	71 (± 3)	8 (± 4)
	0.95H	21.1 (± 5.9)	NA	NA	19 (± 4)	71 (± 3)	10 (± 5)
	Bed	26.7 (± 11.6)	NA	NA	17 (± 5)	65 (± 5)	18 (± 10)
	All samples	16.2 (± 7.6)	NA	NA	24 (± 7)	70 (± 4)	6 (± 6)

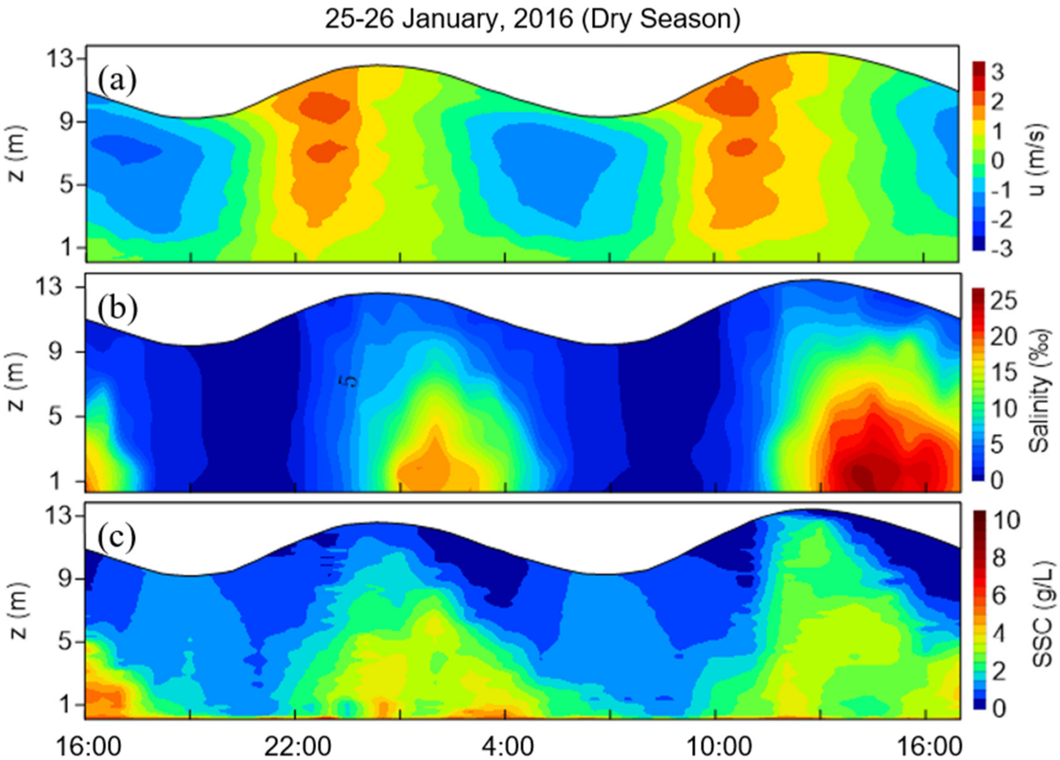

Fig. 11. Time-depth variability of (a) along-channel velocity (u), (b) salinity and (c) SSC during 25–26 January 2016. Positive u indicates the flood direction.

5.4. Intra-tidal SSC variation

Based on many in-situ and laboratory measurements, Maa and Kim (2002) and Ha and Maa (2009) found that erosion only occurs when the tidal current is in acceleration phases. This process may be used in this study to explain the observed intra-tidal SSC variation. Besides, the survey site locates on the land side to the tidally-averaged ETM (Wan, 2015; see Figs. 7–12), and thus horizontal advection may also contribute to the change of SSC time series, because of the large longitudinal and lateral SSC gradient.

During the flood periods in the wet season, the SSC increases with a reasonable pace whenever the current is accelerating (Fig. 6d). This slight increase may be attributed to the re-dispersion of new deposit from previous slack tides and the landward ETM movement. The SSC decreases slightly when the current starts decelerating. The cut-off of sediment supply from the bed and deposition in the late flood are responsible for this decrease. During ebb periods, the SSC jumps (or increases quickly) right after tidal current changes to acceleration phases. It suddenly decreases and recovers in 1–2 h during this phase. There is a strong shoal-to-channel flow (Fig. 6b) for the decreasing SSC, and vice

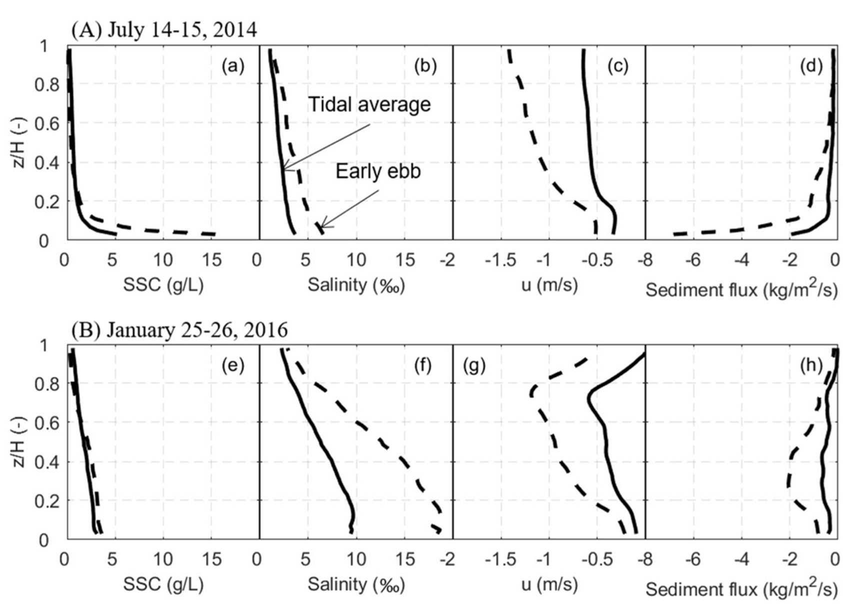

Fig. 12. Profiles of (a) (e) SSC, (b) (f) salinity, (c) (g) along-channel velocity (u) and (d) (h) along-channel sediment flux averaged over tidal cycles (solid line) and early ebb (dash line) of spring tide in July 2014 (upper panels) and January 2016 (lower panels). Negative u and flux indicate the direction from land to sea.

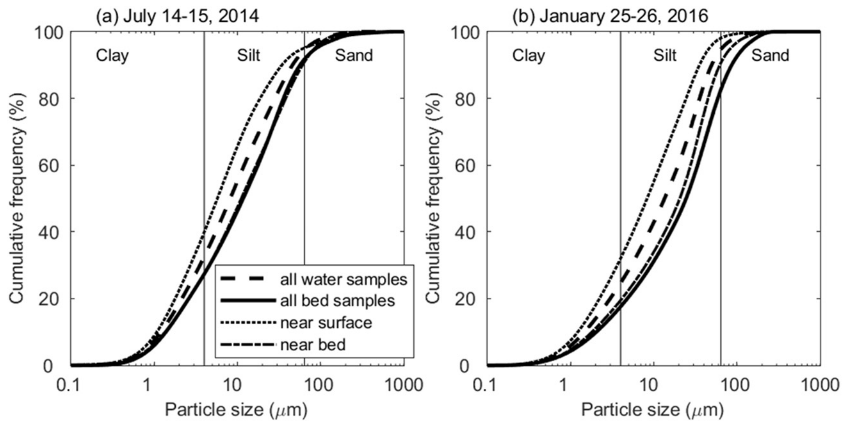

Fig. 13. The cumulative frequency distribution of the sediment samples collected near water surface (dot), near seabed (dash dot), and at seabed surface (solid) in July 2014 (a) and January 2016 (b). The dash line represents the average of all water samples.

versa for the increase. It suggests that lateral flow controls the rapidly increasing or decreasing SSC during these periods. The SSC drops significantly right after the current starts decelerating, and remains about the same then. The withdrawal ETM (i.e., seaward movement) may predominate the rapid decrease, while the constant SSC may be the result of limited sediment supply from the seabed.

In the dry season (Fig. 7c), the changes of SSC during the accelerating flood and the decelerating ebb have a similar pattern to those in the wet season. When the flood currents change to deceleration phases, however, the SSC first keeps increasing and then decreases gradually. During the accelerating ebb, a slight increase occurs in the beginning, followed by a slight decrease. Such variations during these two phases cannot be explained only by the asymmetric erosion/deposition, and longitudinal ETM movement may predominate these changes. Because of the low freshwater discharge, both salinity wedge and ETM can intrude further upstream. The ETM may even pass the observation station, leading to the increasing SSC during the decelerating flood. The decrease during the accelerating ebb may be the result of withdrawal ETM.

The difference between these two survey periods is probably caused by the different location and distribution of ETM. The ETM appears as a concentrated undercurrent in the wet season, and a low concentration sediment cloud in the dry season (Wu et al., 2012). A larger horizontal SSC gradient thus occurs in the wet season, especially in the cross-channel direction. In the branched Yangtze Estuary, the cross-channel current is caused by the barotropic force induced by the cross-shoal flow (Zhu et al., 2018). Although the cross-channel current is roughly the same during these two seasons (Figs. 6b and 7b), it provides a much stronger advective transport of SSC in the wet season, because of the larger SSC gradient. Such cross-channel transport of SSC is even stronger than that from the erosion of bottom sediment. At the ETM, both along- and cross-channel advection contribute significantly to the change of SSC, and thus, the observations of asymmetric erosion/deposition are not as clear as those observed by Maa and Kim (2002). More discussion/studies on the dominant process that controls intratidal SSC variation are needed, which should include detailed data on longitudinal and lateral distributions of ETM and current.

6. Conclusions

This work suggests a combined usage of OBS, ASM, and ADV to detecting large SSC accurately. We successfully solve the ambiguity problem and access a broader measurement range and high-resolution SSC profiles. The ASM-derived SSC is preferred because it has the lowest relative error (~25%). The ASM also provides high-resolution (1 cm) SSC profiles when it is not saturated (SSC < 9 g/L). Once the ASM is saturated, the OBS can be used. Both OBS and ADV can extend their measurement range up to 300 g/L. Although the ADV has a broader SSC range, the best it can be used is to have a rough estimation and assist in the conversion of OBS output. To reduce the effects of particle size, we suggest the usage of in-situ water samples or mixed bottom sediment for the sensor calibration. Alternatively, one can take particle size correction into account in the calibration to access a higher accuracy.

The application of the IOA approach successfully captured and measured the concentrated benthic suspensions (SSC > 10 g/L) in the Yangtze Estuary. Comparison between estimates and the SSC of the in-situ water sample indicates that the IOA approach is reliable and gives estimates with a relative error of 17–34%. The observed SSC profile in the Yangtze Estuary shows a notable seasonal variation. In the wet season, suspended sediment accumulates in the benthic layer, forming a non-uniform L-shaped profile, whereas a uniform and linear profile in the dry season.

Acknowledgments

This work is supported by the project 'Coping with deltas in transition' within the Programme of Strategic Scientific Alliance between China and The Netherlands (PSA), financed by the Ministry of Science and Technology of the People's Republic of China (MOST) (No. 2016YFE0133700) and Royal Netherlands Academy of Arts and Sciences (KNAW) (No. PSA-SA-E-02), and also partly by the National Natural Science Foundation of China (Nos. 51739005; 41876091) and Shanghai Science and Technology Committee (Nos. 18DZ1206400; 19QA1402900). J. Lin is partially supported by the China Scholarship Council (No: 201706140180). We thank J. Gu, J. Zhao, L. Zhu, D. Zhang, C. Guo, Y. Chen, C. Xing, Z. Deng, J. Jiang, Y. Shen, and R. Wu, C. Zhu for their help in the campaign and data analysis and inspiring discussion. We also thank editor Prof. Edward Anthony and two anonymous reviewers for their constructive and helpful comments that help to improve the manuscript.

References

Anastasiou, S., Sylaios, G.K., Tsihrintzis, V.A., 2015. Suspended particulate matter estimates using optical and acoustic sensors: application in Nestos River plume (Thracian Sea, North Aegean Sea). Environ. Monit. Assess. 187. https://doi.org/10.1007/s10661-015-4599-y.

Argus, 2014. User manual: Argus Suspension Meter V. Available Web at. http//argusnet.de/wp-content/uploads/2016/12/asm_V_reference.pdf.

Baeye, M., Fettweis, M., 2015. In situ observations of suspended particulate matter plumes at an offshore wind farm, southern North Sea. Geo-Marine Lett 35, 247–255. https://doi.org/10.1007/s00367-015-0404-8.

Burchard, H., Schuttelaars, H.M., Ralston, D.K., 2018. Sediment trapping in estuaries. Annu. Rev. Mar. Sci. 10https://doi.org/10.1146/annurev-marine-010816-060535. annurev-marine-010816-060535.

Campbell Scientific, I., 2018. Operator's manual: OBS-3A Turbidity and Temperature

Monitoring System. Available Web at. https://s.campbellsci.com/documents/us/manuals/obs-3a.pdf.
Campbell, C.G., Laycak, D.T., Hoppes, W., Tran, N.T., Shi, F.G., 2005. High concentration suspended sediment measurements using a continuous fiber optic in-stream transmissometer. J. Hydrol. 311, 244–253. https://doi.org/10.1016/j.jhydrol.2005.01.026.
Cellino, M., Graf, W.H., 1999. Sediment-laden flow in open-channels under noncapacity and capacity conditions. J. Hydraul. Eng. - ASCE 125, 455–462.
Conner, C.S., De Visser, A.M., 1992. A laboratory investigation of particle size effects on an optical backscatterance sensor. Mar. Geol. 108, 151–159. https://doi.org/10.1016/0025-3227(92)90169-I.
Deng, Z., He, Q., Safar, Z., Chassagne, C., 2019. The role of algae in fine sediment flocculation: in-situ and laboratory measurements. Mar. Geol. 413, 71–84. https://doi.org/10.1016/j.margeo.2019.02.003.
Downing, J., 2006. Twenty-five years with OBS sensors: the good, the bad, and the ugly. Cont. Shelf Res. 26, 2299–2318. https://doi.org/10.1016/j.csr.2006.07.018.
Druine, F., Verney, R., Deloffre, J., Lemoine, J.P., Chapalain, M., Landemaine, V., Lafite, R., 2018. In situ high frequency long term measurements of suspended sediment concentration in turbid estuarine system (Seine Estuary, France): optical turbidity sensors response to suspended sediment characteristics. Mar. Geol. 400, 24–37. https://doi.org/10.1016/j.margeo.2018.03.003.
Fettweis, M., Baeye, M., 2015. Seasonal variation in concentration, size, and settling velocity of muddy marine flocs in the benthic boundary layer. J. Geophys. Res. Ocean. 120, 5648–5667. https://doi.org/10.1002/2014JC010644.
Fugate, D.C., Friedrichs, C.T., 2002. Determining concentration and fall velocity of estuarine particle populations using adv, obs and lisst. Cont. Shelf Res. 22, 1867–1886. https://doi.org/10.1016/S0278-4343(02)00043-2.
Ge, J., Shen, F., Guo, W., Chen, C., Ding, P., 2015. Estimation of critical shear stress for erosion in the Changjiang Estuary: a synergy research of observation, GOCI sensing and modeling. J. Geophys. Res. Ocean. 8439–8465. https://doi.org/10.1002/2015JC010992 2.
Ge, J., Zhou, Z., Yang, W., Ding, P., Chen, C., Wang, Z.B., Gu, J., 2018. Formation of concentrated benthic suspension in a time-dependent salt wedge estuary. J. Geophys. Res. Ocean. 1–27. https://doi.org/10.1029/2018JC013876.
Geyer, W.R., 1993. The importance of suppression of turbulence by stratification on the estuarine turbidity maximum. Estuaries 16, 113–125. https://doi.org/10.1007/BF02690231.
Gibbs, R.J., Wolanski, E., 1992. The effect of flocs on optical backscattering measurements of suspended material concentration. Mar. Geol. 107, 289–291. https://doi.org/10.1016/0025-3227(92)90078-V.
Gray, J.R., Gartner, J.W., 2010. Technological advances in suspended-sediment surrogate monitoring. Water Resour. Res. 46. https://doi.org/10.1029/2008WR007063.
Green, M.O., Boon, J.D., 1993. The measurement of constituent concentrations of non homogenous sediments suspension using optical backscatter sensors. Mar. Geol. 110 (find pages).
Guerrero, M., Szupiany, R.N., Amsler, M., 2011. Comparison of acoustic backscattering techniques for suspended sediments investigation. Flow Meas. Instrum. 22, 392–401. https://doi.org/10.1016/j.flowmeasinst.2011.06.003.
Guo, C., He, Q., Guo, L., Winterwerp, J.C., 2017. A study of in-situ sediment flocculation in the turbidity maxima of the Yangtze Estuary. Estuar. Coast. Shelf Sci. 191, 1–9. https://doi.org/10.1016/j.ecss.2017.04.001.
Guo, C., He, Q., van Prooijen, B.C., Guo, L., Manning, A.J., Bass, S., 2018a. Investigation of flocculation dynamics under changing hydrodynamic forcing on an intertidal mudflat. Mar. Geol. 395, 120–132. https://doi.org/10.1016/j.margeo.2017.10.001.
Guo, L., Su, N., Zhu, C., He, Q., 2018b. How have the river discharges and sediment loads changed in the Changjiang River basin downstream of the Three Gorges Dam? J. Hydrol. 560, 259–274. https://doi.org/10.1016/j.jhydrol.2018.03.035.
Ha, H.K., Maa, J.P.Y., 2009. Evaluation of two conflicting paradigms for cohesive sediment deposition. Mar. Geol. 265, 120–129. https://doi.org/10.1016/j.margeo.2009.07.001.
Ha, H.K., Hsu, W.Y., Maa, J.P.Y., Shao, Y.Y., Holland, C.W., 2009. Using ADV backscatter strength for measuring suspended cohesive sediment concentration. Cont. Shelf Res. 29, 1310–1316. https://doi.org/10.1016/j.csr.2009.03.001.
Ha, H.K., Maa, J.P.Y., Park, K., Kim, Y.H., 2011. Estimation of high-resolution sediment concentration profiles in bottom boundary layer using pulse-coherent acoustic Doppler current profilers. Mar. Geol. 279, 199–209. https://doi.org/10.1016/j.margeo.2010.11.002.
He, Q., Li, J.F., Li, Y., Jin, X.S., Che, Y., 2001. Field measurements of bottom boundary layer processes and sediment resuspension in the Changjiang Estuary. Sci. China Ser. B-Chemistry 44, 80–86. https://doi.org/10.1007/Bf02884812.
Huettel, M., Berg, P., Kostka, J.E., 2014. Benthic exchange and biogeochemical cycling in permeable sediments. Annu. Rev. Mar. Sci. 6, 23–51. https://doi.org/10.1146/annurev-marine-051413-012706.
Kineke, G.C., Sternberg, R.W., 1992. Measurements of high concentration suspended sediments using the optical backscatterance sensor. Mar. Geol. 108, 253–258. https://doi.org/10.1016/0025-3227(92)90199-R.
Liang, D., Wang, X., Bockelmann-Evans, B.N., Falconer, R.A., 2013. Study on nutrient distribution and interaction with sediments in a macro-tidal estuary. Adv. Water Resour. 52, 207–220. https://doi.org/10.1016/J.ADVWATRES.2012.11.015.
Ludwig, K.A., Hanes, D.M., 1990. A laboratory evaluation of optical backscatterance suspended solids sensors exposed to sand-mud mixtures. Mar. Geol. 94, 173–179. https://doi.org/10.1016/0025-3227(90)90111-V.
Maa, J.P.Y., Kim, S.C., 2002. A constant erosion rate model for fine sediment in the York River, Virginia. Environ. Fluid Mech. 1, 345–360. https://doi.org/10.1023/A:1015799926777.
Maa, J.P.Y., Xu, J., Victor, M., 1992. Notes on the performance of an optical backscatter sensor for cohesive sediments. Mar. Geol. 104, 215–218. https://doi.org/10.1016/0025-3227(92)90096-Z.
Manning, A.J., Langston, W.J., Jonas, P.J.C., 2010. A review of sediment dynamics in the Severn Estuary: influence of flocculation. Mar. Pollut. Bull. 61, 37–51. https://doi.org/10.1016/j.marpolbul.2009.12.012.
McHenry, J.R., Coleman, N.L., Willis, J.C., Murphree, C.E., Bolton, G.C., Sansom, O.W., Gill, A.C., 1967. Performance of nuclear-sediment concentration gauges. Isot. Hydrol. 38, 207–225.
Merckelbach, L.M., Ridderinkhof, H., 2006. Estimating suspended sediment concentration using backscatterance from an acoustic Doppler profiling current meter at a site with strong tidal currents. Ocean Dyn. 56, 153–168. https://doi.org/10.1007/s10236-005-0036-z.
Merten, G.H., Capel, P.D., Minella, J.P.G., 2014. Effects of suspended sediment concentration and grain size on three optical turbidity sensors. J. Soils Sediments 14, 1235–1241. https://doi.org/10.1007/s11368-013-0813-0.
Moura, M.G., Quaresma, V.S., Bastos, A.C., Veronez, P., 2011. Field observations of SPM using ADV, ADP, and OBS in a shallow estuarine system with low SPM concentration-Vitória Bay, SE Brazil. Ocean Dyn. 61, 273–283. https://doi.org/10.1007/s10236-010-0364-5.
Nauw, J.J., Merckelbach, L.M., Ridderinkhof, H., van Aken, H.M., 2014. Long-term ferry-based observations of the suspended sediment fluxes through the Marsdiep inlet using acoustic Doppler current profilers. J. Sea Res. 87, 17–29. https://doi.org/10.1016/j.seares.2013.11.013.
Nortek, A.S., 2005. Technical specification: Vector-300m. Available on Web at. https://www.nortekgroup.com/export/pdf/Vector%20-%20300%20m.pdf.
Rai, A.K., Kumar, A., 2015. Continuous measurement of suspended sediment concentration: technological advancement and future outlook. Meas. J. Int. Meas. Confed. 76, 209–227. https://doi.org/10.1016/j.measurement.2015.08.013.
Rymszewicz, A., O'Sullivan, J.J., Bruen, M., Turner, J.N., Lawler, D.M., Conroy, E., Kelly-Quinn, M., 2017. Measurement differences between turbidity instruments, and their implications for suspended sediment concentration and load calculations: a sensor inter-comparison study. J. Environ. Manag. 199, 99–108. https://doi.org/10.1016/j.jenvman.2017.05.017.
Sahin, C., Safak, I., Hsu, T.J., Sheremet, A., 2013. Observations of suspended sediment stratification from acoustic backscatter in muddy environments. Mar. Geol. 336, 24–32. https://doi.org/10.1016/j.margeo.2012.12.001.
Salehi, M., Strom, K., 2011. Using velocimeter signal to noise ratio as a surrogate measure of suspended mud concentration. Cont. Shelf Res. 31, 1020–1032. https://doi.org/10.1016/j.csr.2011.03.008.
Scheu, K.R., Fong, D.A., Monismith, S.G., Fringer, O.B., 2015. Sediment transport dynamics near a river inflow in a large alpine lake. Limnol. Oceanogr. 60, 1195–1211. https://doi.org/10.1002/lno.10089.
Shao, Y., Maa, J., 2017. Comparisons of different instruments for measuring suspended cohesive sediment concentrations. Water 9, 968. https://doi.org/10.3390/w9120968.
Shi, J.Z., Zhang, S.Y., Hamilton, L.J., 2006. Bottom fine sediment boundary layer and transport processes at the mouth of the Changjiang Estuary, China. J. Hydrol. 327, 276–288. https://doi.org/10.1016/j.jhydrol.2005.11.039.
Simpson, J.H., Brown, J., Matthews, J., Allen, G., 1990. Tidal straining, density currents, and stirring in the control of estuarine stratification. Estuaries 13, 125. https://doi.org/10.2307/1351581.
Song, D., Wang, X.H., Cao, Z., Guan, W., 2013. Suspended sediment transport in the Deepwater Navigation Channel, Yangtze River Estuary, China, in the dry season 2009: 1. Observations over spring and neap tidal cycles. J. Geophys. Res. Ocean. 118, 5555–5567. https://doi.org/10.1002/jgrc.20410.
Su, M., Yao, P., Wang, Z., Zhang, C., Chen, Y., Stive, M.J.F., 2016. Conversion of electro-optical signals to sediment concentration in a silt–sand suspension environment. Coast. Eng. 114, 284–294. https://doi.org/10.1016/j.coastaleng.2016.04.014.
Thorne, P.D., Hanes, D.M., 2002. A review of acoustic measurement of small-scale sediment processes. Cont. Shelf Res. 22, 603–632. https://doi.org/10.1016/S0278-4343(01)00101-7.
Van Kessel, T., Winterwerp, H., Van Prooijen, B., Van Ledden, M., Borst, W., 2011. Modelling the seasonal dynamics of SPM with a simple algorithm for the buffering of fines in a sandy seabed. Cont. Shelf Res. 31, S124–S134. https://doi.org/10.1016/j.csr.2010.04.008.
Vijverberg, T., Winterwerp, J.C., Aarninkhof, S.G.J., Drost, H., 2011. Fine sediment dynamics in a shallow lake and implication for design of hydraulic works. Ocean Dyn. 61, 187–202. https://doi.org/10.1007/s10236-010-0322-2.
Wan, Y., 2015. Multiscale Physical Processes of Fine Sediment in an Estuary (PhD Thesis). Delft University of Technology, The Netherlands (198 pp.).
Wan, Y., Roelvink, D., Li, W., Qi, D., Gu, F., 2014. Observation and modeling of the storm-induced fluid mud dynamics in a muddy-estuarine navigational channel. Geomorphology 217, 23–36. https://doi.org/10.1016/j.geomorph.2014.03.050.
Wang, Y.P., Voulgaris, G., Li, Y., Yang, Y., Gao, J., Chen, J., Gao, S., 2013. Sediment resuspension, flocculation, and settling in a macrotidal estuary. J. Geophys. Res. Ocean. 118, 5591–5608. https://doi.org/10.1002/jgrc.20340.
Winterwerp, J.C., Lely, M., He, Q., 2009. Sediment-induced buoyancy destruction and drag reduction in estuaries. Ocean Dyn. 59, 781–791. https://doi.org/10.1007/s10236-009-0237-y.
Winterwerp, J.C., Vroom, J., Wang, Z.B., Krebs, M., Hendriks, E.C.M., van Maren, D.S., Schrottke, K., Borgsmüller, C., Schöl, A., 2017. SPM response to tide and river flow in the hyper-turbid Ems River. Ocean Dyn. 67, 559–583. https://doi.org/10.1007/s10236-017-1043-6.
Wren, B.D.G., Barkdoll, B.D., Kuhnle, R. a, Derrow, R.W., 2000. Field techniques for suspended-sediment measurement. J. Hydraul. Eng. 126, 97–104.
Wu, J., Liu, J.T., Wang, X., 2012. Sediment trapping of turbidity maxima in the

Changjiang Estuary. Mar. Geol. 303–306, 14–25. https://doi.org/10.1016/j.margeo.2012.02.011.
Yang, Y., Wang, Y.P., Gao, S., Wang, X.H., Shi, B.W., Zhou, L., Wang, D.D., Dai, C., Li, G.C., 2016. Sediment resuspension in tidally dominated coastal environments: new insights into the threshold for initial movement. Ocean Dyn. 66, 401–417. https://doi.org/10.1007/s10236-016-0930-6.
Yoshiyama, K., Sharp, J.H., 2006. Phytoplankton response to nutrient enrichment in an urbanized estuary: apparent inhibition of primary production by overeutrophication. Limnol. Oceanogr. 51, 424–434. https://doi.org/10.4319/lo.2006.51.1_part_2.0424.
YSI Incorporated, 2012. User manual: 6-Series, Multiparameter Water Quality Sondes. Available Web at. https://www.ysi.com/File%20Library/Documents/Manuals/069300-YSI-6-Series-Manual-RevJ.pdfpp. 374.
Zhu, L., He, Q., Shen, J., 2018. Modeling lateral circulation and its influence on the along-channel flow in a branched estuary. Ocean Dyn. 68, 177–191. https://doi.org/10.1007/s10236-017-1114-8.